
Direct Observation of the Two-Plasmon–Decay Common Plasma Wave Using Ultraviolet Thomson Scattering

The self-organization of nonlinearly interacting dynamic systems into coherent synchronized states has attracted a broad interest across a range of subject areas in the biological and physical sciences.¹ Within plasma physics, multibeam laser facilities present the opportunity for synchronization of parametric instabilities driven by intense laser beams propagating through a long-scale-length plasma. Two-plasmon decay (TPD) is a three-wave parametric instability in which an electromagnetic wave decays into two electron plasma waves (EPW's),² and when multiple laser beams are used, their interactions with EPW's can be synchronized by phase coupling to common decay waves. This leads to a reduction in the single-beam intensity required to drive the TPD instability above the linear threshold.³

Numerical simulations predict that once the TPD instability is driven above the linear threshold, EPW's rapidly reach amplitudes where secondary processes such as the Langmuir decay instability (LDI)⁴ and cavitation lead to a broad EPW spectrum.^{5,6} This broad EPW spectrum can stochastically accelerate electrons from the bulk velocity distribution to high energies (>30 keV) (Refs. 7 and 8).

Early multibeam experiments showed evidence of TPD-generated hot electrons when the single-beam growth rates were significantly below threshold. These studies showed that TPD hot-electron generation was governed by the overlapped drive intensity;⁹ subsequent experiments showed that hot-electron generation scaled with the maximum multibeam growth rate.¹⁰ These studies used indirect measurements of TPD that were dependent on nonlinear processes associated with TPD saturation, which challenges the validity of comparing to linear TPD theory. Thomson scattering of the drive laser beams (self-Thomson scattering) provides a more-direct signature of TPD-driven EPW's,¹¹ and the spectral features have been discussed in theoretical studies of TPD-driven LDI.¹² Quantitative comparison has been limited by the difficulty in defining the EPW's that are probed when using large numbers of drive beams.^{13,14} Very early laser-plasma experiments made the most-direct experimental observations of TPD by using a

Thomson-scattering probe to observe the amplitude, which is proportional to the square root of the scattered power and the frequency of EPW's driven by a single CO₂ laser.^{15,16}

This article presents the direct observation of TPD waves and associated Langmuir decay daughter waves driven by multiple laser beams. An ultraviolet Thomson-scattering probe beam was used to isolate EPW's driven by multibeam TPD, which allowed for a quantitative comparison of the results with three-dimensional (3-D) numerical simulations that account for the nonlinear nature of the instability and the multibeam geometry used in the experiments. The narrow width [1.6 ± 0.1 -nm full width at half maximum (FWHM)] and peak wavelength (423.1 ± 0.2 nm) of the common-wave scattering feature show that the EPW's are driven near the region of maximum common-wave growth. When a fixed overlapped intensity was maintained, the plasma-wave amplitudes were nearly independent of the number of drive beams, demonstrating that these EPW's are driven by multiple laser beams. A broad (3.1 ± 0.5 -nm FWHM) Thomson-scattering feature driven by TPD was observed while probing a range of wave vectors that did not include primary common EPW's. A second peak, corresponding to Langmuir decay of primary TPD EPW's, was observed in the Thomson-scattering spectra, suggesting that LDI is responsible for the observed broad range of driven EPW's. The measured Thomson-scattering spectra were well reproduced by 3-D numerical simulations, suggesting that the simulations accurately model the EPW amplitudes in this highly nonlinear system.

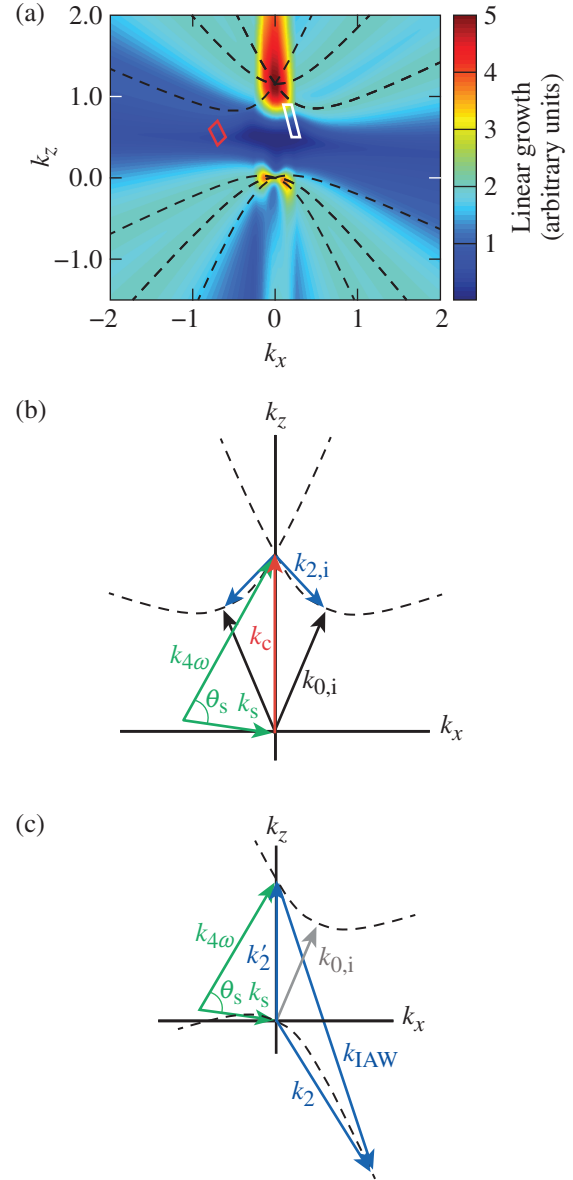
The experiments were conducted on the OMEGA Laser System¹⁷ and used two to five $\lambda_{3\omega} = 351$ -nm laser beams to drive common EPW's. The beams were incident on a planar target with an angle of 23° with respect to the target normal. Phase plates¹⁸ were used on each beam to define the $300\text{-}\mu\text{m}$ FWHM flat-top laser spots. Prior to being focused by an $f/6.7$ lens, the beams propagated through a birefringent polarization smoothing crystal that separated the incident linearly polarized laser beam into two overlapped beams with orthogonal polarizations propagating at a slight angle (~ 40 μrad). The laser beams used

1-ns- or 2-ns-long square pulses with the same energy in each beam. When the number of beams and pulse lengths were varied, the laser energies were adjusted to maintain a constant vacuum overlapped intensity ($\sim 10^{15}$ W/cm²), resulting in the same hydrodynamic conditions for all experiments. The planar targets were 3-mm \times 3-mm squares consisting of 30- μ m-thick CH layers coated on 30- μ m-thick Mo. The CH-layer thickness was chosen such that the burnthrough time was much longer than the laser pulse.¹⁹

The Thomson-scattering diagnostic consisted of a $\lambda_{4\omega} = 263.25$ -nm $f/6.7$ probe beam with a best-focus diameter of ~ 50 μ m (Ref. 20). The Thomson-scattered light was collected by a reflective $f/10$ collection system coupled to two spectrometer/streak cameras, used to simultaneously observe the EPW and ion-acoustic wave (IAW) scattering features.²¹ The spectral resolutions of the IAW and EPW systems are 0.05 nm and 0.5 nm, respectively. Scattered light was collected from an $\sim 50 \times 50 \times 50$ - μ m³ volume located either 150 μ m ($n_e/n_c \approx 0.18$ to 0.21) or 100 μ m ($n_e/n_c \approx 0.21$ to 0.25) from the target surface (where n_e is the electron density and n_c is the critical density for 351-nm light). The angle between the collection optic and probe beam was 120°. Two Thomson-scattering geometries were used to probe plasma wave vectors near the region of maximum common-wave growth (common-wave configuration) and a region where there was no linear common-wave coupling (non-common-wave configuration). The range of wave vectors probed in the two configurations [Fig. 141.1(a)] was calculated by ray tracing through density profiles generated using the two-dimensional (2-D) hydrodynamic code *DRACO*, where the electron heat flux was limited to 6% of the free-streaming flux.²² Refraction reduced the scattering angle in the plasma to $\theta_s^{cw} \approx 32^\circ$ and $\theta_s^{ncw} \approx 55^\circ$ in the common-wave and non-common-wave configurations, respectively.

The TPD linear theory with multiple laser beams predicts a maximum growth rate along the axis of symmetry defined by the laser beams [the z axis in Fig. 141.1(a)].³ The frequency ($\omega_0 = \omega_1 + \omega_2$) and wave vector ($\mathbf{k}_0 = \mathbf{k}_1 + \mathbf{k}_2$) matching conditions and linear EPW dispersion relation ($\omega_{1,2}^2 = \omega_{pe}^2 + 3k_{1,2}^2 v_{te}^2$) can be satisfied for multiple beams sharing a common daughter wave only when they share a common angle relative to the driven wave [where $(\omega_{1,2}, \mathbf{k}_{1,2})$ are the daughter EPW frequencies and wave vectors, (ω_0, \mathbf{k}_0) are the drive-beam frequency and wave vector, $\omega_{pe} = \omega_0 \sqrt{n_e/n_c}$ is the electron plasma frequency, and $v_{te} = \sqrt{T_e/m_e}$ is the electron thermal velocity (m_e is the electron mass)].

In experiments where multiple beams share a common azimuthal angle, the maximum linear growth rate occurs at the



E23766JR

Figure 141.1

(a) The normalized five-beam common-wave growth rate (color scale) in the Thomson-scattering plane [defined by $\hat{y} \parallel (\hat{k}_{4\omega} \times \hat{k}_s)$ with the target normal in the $-\hat{z}$ direction]. The dashed curves show the linear two-plasmon-decay (TPD) theory maximum growth for each drive beam. The white (red) box shows the range of wave vectors probed by the Thomson-scattering diagnostic in the common-wave (non-common-wave) configuration. (b) Wave-matching conditions for Thomson scattering ($\mathbf{k}_c = \mathbf{k}_{4\omega} - \mathbf{k}_s$) from common TPD electron plasma waves (EPW's); (c) daughter EPW's from Langmuir decay of backscattered TPD EPW's ($\mathbf{k}'_2 = \mathbf{k}_2 - \mathbf{k}_{IAW} = \mathbf{k}_{4\omega} - \mathbf{k}_s$).

intersection of the single-beam maximum growth rates, which lies along hyperboloids $[k_{\perp} = k_{\parallel}(k_{\parallel} - k_0)]$ (where k_{\perp} and k_{\parallel} are the components of the plasma-wave vector perpendicular and parallel to the drive-beam wave vector, respectively).¹⁰ Electron plasma waves corresponding to distinct branches of a hyperboloid are categorized as forward scattered ($\omega_1 > \omega_0/2$, $\mathbf{k}_1 \cdot \mathbf{k}_0 > 0$) or backscattered ($\omega_2 > \omega_0/2$, $\mathbf{k}_2 \cdot \mathbf{k}_0 > 0$). Figure 141.1(b) shows the wave-vector-matching condition for Thomson scattering from forward-scattered common TPD EPW's $\mathbf{k}_c = \mathbf{k}_{4\omega} - \mathbf{k}_s$ (where $\mathbf{k}_{4\omega}$, \mathbf{k}_s , and \mathbf{k}_c are the wave vectors of the probe beam, Thomson-scattered light, and common EPW, respectively). The associated matching conditions and dispersion relations predict a Thomson-scattered peak wavelength of $\lambda_{s,c} = 423 \pm 0.5$ nm.

Figure 141.2(a) shows a broad (9.1 ± 1.1 -nm FWHM) EPW Thomson-scattering spectrum measured $150 \mu\text{m}$ from the initial target surface. The scattering feature has a single spectral peak with a shape consistent with the intensity distribution of the probe beam, indicating that thermal EPW's of roughly equal amplitudes are present throughout the (physical) scattering volume. The observed peak corresponds to Thomson scattering from EPW's from a range of densities $n_e/n_c \approx 0.18$ to 0.21 . The IAW spectrum was fit to the collisionless dynamic structure factor, giving a measure of the electron temperature ($T_e = 2.0 \pm 0.2$ keV at 1 ns) and plasma flow velocity along the target normal ($v_f = 5.5 \pm 0.5 \times 10^7$ cm/s) (Ref. 23). The simulated values of $T_e = 1.9$ keV and $v_f = 5 \times 10^7$ cm/s from *DRACO* agree with the measurements.

Figure 141.2(b) shows a narrow (1.6 ± 0.1 -nm FWHM) high-intensity feature that appears at a wavelength ($\lambda_s = 423.1 \pm 0.2$ nm) consistent with the common-wave model ($\lambda_{s,c} = 423 \pm 0.5$ nm). The peak is an order of magnitude more intense and $\sim 10\times$ narrower than the thermal peak [presumably below the detection level in Fig. 141.2(b)], showing the driven nature of the waves. The wavelength range corresponds to Thomson scattering from densities between $n_e/n_c \approx 0.246$ and 0.247 . This is much narrower than the range of densities in the scattering volume ($n_e/n_c \approx 0.21$ to 0.25), indicating that the peak corresponds to locally driven EPW's.

The integrated Thomson-scattered power in the common-wave configuration (proportional to the square root of the wave amplitude) was nearly independent of the number of drive beams when maintaining a constant overlapped intensity. For two-, three-, and five-beam experiments, the relative Thomson-scattered power scaled by 1, 0.7, and 0.5, respectively. The same scaling (within $\sim 10\%$) was observed in simultaneous hard x-ray measurements, consistent with the expected correlation between hard x-ray generation and TPD-driven EPW amplitudes.¹³ The small amplitude variation with the number of beams at a fixed overlapped intensity and the narrow spectral width shows that the observed peak corresponds to Thomson scattering from common TPD EPW's.

The shorter-wavelength peak ($\lambda_s = 413.7 \pm 0.2$ nm) shown in Fig. 141.2(b) corresponds to Thomson scattering from

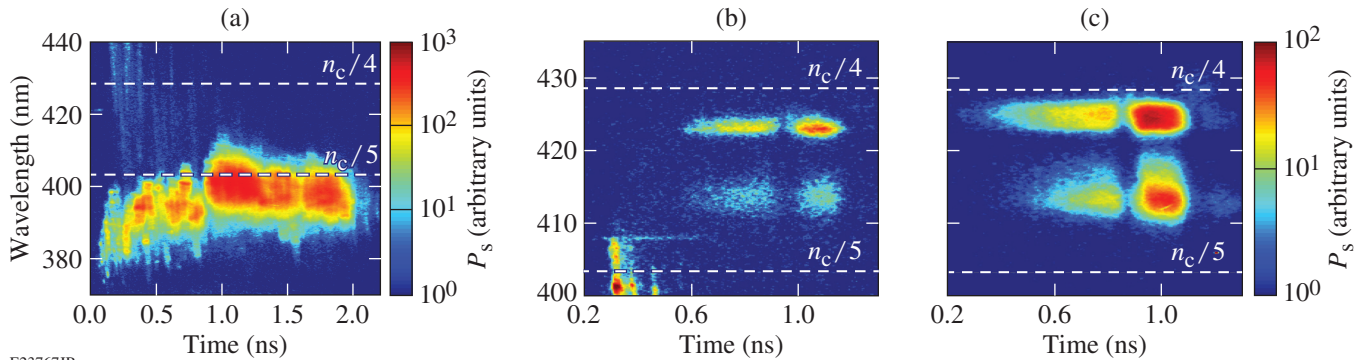
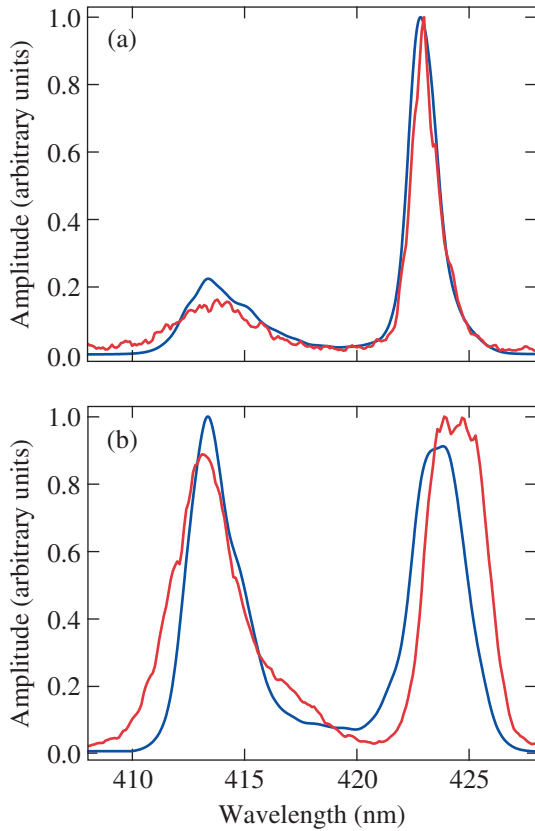


Figure 141.2

Thomson-scattering spectra for scattering from EPW's with dashed lines at wavelengths corresponding to the quarter ($n_c/4$)- and fifth ($n_c/5$)-critical surfaces. (a) Scattering from thermal EPW's ($150 \mu\text{m}$ from target surface) generates a broad spectrum corresponding to the range of densities within the Thomson-scattering volume. (b) Scattering spectra from common EPW's ($100 \mu\text{m}$ from target surface) show narrow peaks corresponding to locally driven TPD EPW's. (c) Off-hyperbola scattering ($100 \mu\text{m}$ from target surface) results in a broad spectrum of TPD-driven EPW's. The dip in scattering amplitude at 0.9 ns in all three spectra is caused by a shock, reflected from the Mo layer, traveling through the Thomson-scattering volume.

EPW's driven by Langmuir decay of backscattered TPD EPW's. Figure 141.1(c) shows the wave-matching condition for Thomson scattering from secondary backscattered EPW's (\mathbf{k}'_2), where the blue triangle satisfies the LDI-matching conditions ($\mathbf{k}_2 = \mathbf{k}'_2 + \mathbf{k}'_{IAW}$, $\omega_2 = \omega_2 + \omega_{IAW}$). Assuming that the observed EPW's correspond to direct LDI backscatter ($k_2 = k_{IAW} - k'_2$), the matching conditions and dispersion relations give $\lambda_s = 413.8 \pm 0.3$ nm for Thomson scattering from secondary backscattered EPW's, in agreement with the observed peak.

Figure 141.3(a) compares the measured [Fig. 141.2(b)] and simulated Thomson-scattering spectra from the five-beam common-wave geometry. The simulated peak widths and amplitude ratio are in excellent agreement with the experiment. The simulation parameters were taken from *DRACO* profiles: $T_e = 1.9$ keV, $(In_c/4 = 6 \times 10^{14}$ W/cm²), $L_n = 190$ μ m (density scale length), $T_1 = 1$ keV, $v_{flow} = 5.15 \times 10^7$ cm/s, and



E23768JR

Figure 141.3
Thomson-scattering spectrum measured (red curve) at ~ 1 ns and simulated (blue curve) in the (a) common-wave and (b) non-common-wave Thomson-scattering configurations.

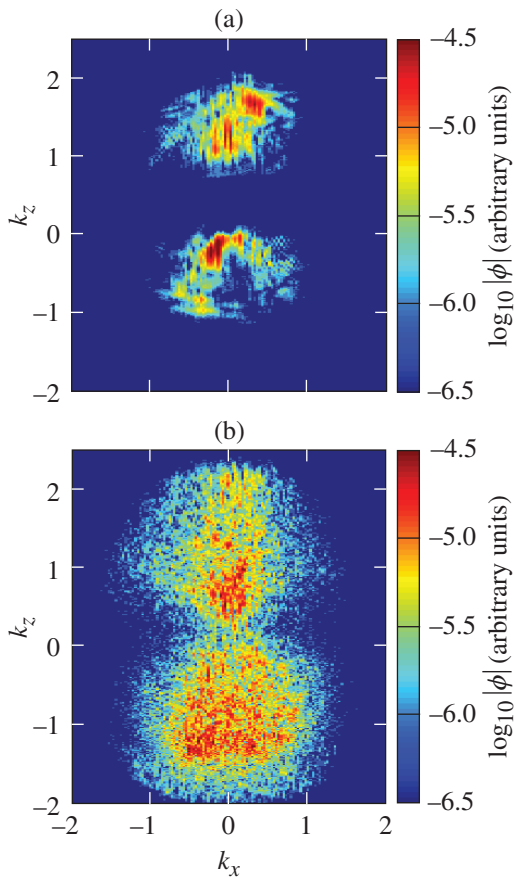
$n_e(z) = n_0 \left[1 - (z/L_n)^{1.12} \right]$, where $n_e(z)$ is a power law fit to the unperturbed electron density profile near $(n_c/4)$ and $n_0 = 0.27 n_c$ is the peak electron density in the simulation box.

The spectra were simulated using a 3-D numerical plasma fluid code (*LPSE*²⁴) that solves the extended Zakharov equations of TPD^{12,25} for the low-frequency IAW's and high-frequency (enveloped) EPW's. The Zakharov equations are used to model the nonlinear coupling between EPW's and IAW's.⁸ Phase plates with polarization smoothing were modeled by splitting each incident beam cone into two sets of 100 cross-polarized plane-wave beamlets with a 40- μ rad angular divergence and random phase. The simulation box was $66 \times 13 \times 13$ μ m³ on a uniform $1300 \times 256 \times 256$ Cartesian grid. Thomson-scattering spectra are generated using a numerical structure factor obtained from simulated time series.

In *LPSE* simulations, the shorter-wavelength Thomson-scattering peak was correlated to the Langmuir decay of backward-propagating TPD EPW's by comparing the temporal evolution of the Thomson-scattering spectrum and the low-frequency density perturbations (IAW's). Figure 141.4(a) shows the simulated EPW spectrum at 1 ps, when the TPD instability was in the linear growth stage; large-amplitude EPW's corresponding to the maximum five-beam common-wave growth rate are the dominant spectral feature. At this time, the corresponding IAW spectrum has no driven waves, and only the peak corresponding to forward-scattered TPD EPW's is observed in the simulated Thomson-scattering spectrum. When the ponderomotive force associated with the electric field of counter-propagating EPW's is sufficient to overcome IAW damping, a series of Langmuir decays generate large-amplitude IAW's, leading to broad IAW and EPW spectra [Fig. 141.4(b)]. At this time (~ 2 ps), the simulated EPW Thomson-scattering spectrum shows two spectral peaks at wavelengths corresponding to forward- and backscattered TPD EPW's.

In simulations where the intensity was just above the threshold for the onset of the TPD instability ($In_c/4 = 2 \times 10^{14}$ W/cm²), the EPW amplitudes did not reach sufficient amplitudes to drive large-amplitude IAW's, and the EPW spectrum looks similar to Fig. 141.4(a) at all times. The spectral peak corresponding to backscattered TPD EPW's never appears in the low-intensity simulated Thomson-scattering spectra, consistent with these EPW's being generated by LDI.

Figure 141.2(c) shows a Thomson-scattering spectrum measured in the non-common-wave geometry [red box in Fig. 141.1(a)], which was chosen such that the Thomson-



E23769JR

Figure 141.4
 Simulated EPW spectra for five drive beams (a) during linear TPD growth (1 ps) and (b) after saturation (2 ps), where ϕ is the high-frequency (enveloped) potential.

scattering diagnostic probes wave vectors that do not satisfy the common-wave matching conditions but is measuring light scattered from a range of densities ($n_e/n_c \approx 0.21$ to 0.25), where TPD is active. The simulated spectrum [Fig. 141.3(b)] is in good agreement with the measured peak widths and relative amplitudes. The small discrepancy observed between the simulated and measured peak wavelengths could be a result of an $\sim 10\%$ underestimation of the electron temperature or an overestimation of the effects of refraction. For a given scattering geometry (i.e., fixed θ_s), the location of the peaks is determined by the electron temperature and their separation is approximately linear in electron temperature.

In summary, common TPD EPW's were observed using ultraviolet Thomson scattering. The common-wave Thomson-scattering feature is characterized by its narrow width (1.6 nm) and weak amplitude scaling with overlapped drive-beam inten-

sity. The observation of EPW's driven by LDI experimentally shows the nonlinear state of the TPD instability and suggests that LDI is responsible for generating a broad EPW spectrum. These results are supported by 3-D LPSE simulations that quantitatively reproduce the experimental scattering spectra.

ACKNOWLEDGMENT

This material is based upon work supported by the Department of Energy National Nuclear Security Administration under Award Number DE-NA0001944, the University of Rochester, and the New York State Energy Research and Development Authority. The support of DOE does not constitute an endorsement by DOE of the views expressed in this article.

REFERENCES

1. A. Pikovsky, M. Rosenblum, and J. Kurths, *Synchronization: A Universal Concept in Nonlinear Sciences* (Cambridge University Press, Cambridge, 2001).
2. E. A. Jackson, Phys. Rev. **153**, 235 (1967).
3. D. T. Michel, A. V. Maximov, R. W. Short, S. X. Hu, J. F. Myatt, W. Seka, A. A. Solodov, B. Yaakobi, and D. H. Froula, Phys. Rev. Lett. **109**, 155007 (2012).
4. D. F. DuBois and M. V. Goldman, Phys. Rev. **164**, 207 (1967).
5. H. X. Vu, D. F. DuBois, D. A. Russell, and J. F. Myatt, Phys. Plasmas **17**, 072701 (2010).
6. J. Meyer and Y. Zhu, Phys. Rev. Lett. **71**, 2915 (1993).
7. R. Yan, C. Ren, J. Li, A. V. Maximov, W. B. Mori, Z.-M. Sheng, and F. S. Tsung, Phys. Rev. Lett. **108**, 175002 (2012).
8. J. F. Myatt, H. X. Vu, D. F. DuBois, D. A. Russell, J. Zhang, R. W. Short, and A. V. Maximov, Phys. Plasmas **20**, 052705 (2013).
9. C. Stoeckl, R. E. Bahr, B. Yaakobi, W. Seka, S. P. Regan, R. S. Craxton, J. A. Delettrez, R. W. Short, J. Myatt, A. V. Maximov, and H. Baldis, Phys. Rev. Lett. **90**, 235002 (2003).
10. D. T. Michel, A. V. Maximov, R. W. Short, J. A. Delettrez, D. Edgell, S. X. Hu, I. V. Igumenshchev, J. F. Myatt, A. A. Solodov, C. Stoeckl, B. Yaakobi, and D. H. Froula, Phys. Plasmas **20**, 055703 (2013).
11. W. Seka, J. F. Myatt, R. W. Short, D. H. Froula, J. Katz, V. N. Goncharov, and I. V. Igumenshchev, Phys. Rev. Lett. **112**, 145001 (2014).
12. D. A. Russell and D. F. DuBois, Phys. Rev. Lett. **86**, 428 (2001).
13. W. Seka, D. H. Edgell, J. F. Myatt, A. V. Maximov, R. W. Short, V. N. Goncharov, and H. A. Baldis, Phys. Plasmas **16**, 052701 (2009).
14. R. L. Berger and L. V. Powers, Phys. Fluids **28**, 2895 (1985).
15. J. J. Schuss, T. K. Chu, and L. C. Johnson, Phys. Rev. Lett. **40**, 27 (1978).
16. H. A. Baldis, J. C. Samson, and P. B. Corkum, Phys. Rev. Lett. **41**, 1719 (1978).

17. T. R. Boehly, R. S. Craxton, T. H. Hinterman, J. H. Kelly, T. J. Kessler, S. A. Kumpan, S. A. Letzring, R. L. McCrory, S. F. B. Morse, W. Seka, S. Skupsky, J. M. Soures, and C. P. Verdon, *Rev. Sci. Instrum.* **66**, 508 (1995).
18. T. J. Kessler, Y. Lin, J. J. Armstrong, and B. Velazquez, in *Laser Coherence Control: Technology and Applications*, edited by H. T. Powell and T. J. Kessler (SPIE, Bellingham, WA, 1993), Vol. 1870, pp. 95–104.
19. B. Yaakobi, P.-Y. Chang, A. A. Solodov, C. Stoeckl, D. H. Edgell, R. S. Craxton, S. X. Hu, J. F. Myatt, F. J. Marshall, W. Seka, and D. H. Froula, *Phys. Plasmas* **19**, 012704 (2012).
20. A. J. Mackinnon, S. Shiromizu, G. Antonini, J. Auerbach, K. Haney, D. H. Froula, J. Moody, G. Gregori, C. Constantin, C. Sorce, L. Divol, R. L. Griffith, S. Glenzer, J. Satariano, P. K. Whitman, S. N. Locke, E. L. Miller, R. Huff, K. Thorp, W. Armstrong, W. Bahr, W. Seka, G. Pien, J. Mathers, S. Morse, S. Loucks, and S. Stagnitto, *Rev. Sci. Instrum.* **75**, 3906 (2004).
21. J. Katz, R. Boni, C. Sorce, R. Follett, M. J. Shoup III, and D. H. Froula, *Rev. Sci. Instrum.* **83**, 10E349 (2012).
22. P. B. Radha, V. N. Goncharov, T. J. B. Collins, J. A. Delettrez, Y. Elbaz, V. Yu. Glebov, R. L. Keck, D. E. Keller, J. P. Knauer, J. A. Marozas, F. J. Marshall, P. W. McKenty, D. D. Meyerhofer, S. P. Regan, T. C. Sangster, D. Shvarts, S. Skupsky, Y. Srebro, R. P. J. Town, and C. Stoeckl, *Phys. Plasmas* **12**, 032702 (2005).
23. D. H. Froula, S. H. Glenzer, N. C. Luhmann, and J. Sheffield, *Plasma Scattering of Electromagnetic Radiation: Theory and Measurement Techniques*, 2nd ed. (Academic Press, Burlington, MA, 2011).
24. J. F. Myatt, J. Shaw, J. Zhang, A. V. Maximov, R. W. Short, W. Seka, D. H. Edgell, D. F. Dubois, D. A. Russell, and H. X. Vu, *Bull. Am. Phys. Soc.* **59**, 241 (2014).
25. D. F. DuBois, D. A. Russell, and H. A. Rose, *Phys. Rev. Lett.* **74**, 3983 (1995).